Journal of Low Temperature Physics (2026) 222:39
https://doi.org/10.1007/s10909-026-03364-0

Development of Superfluid Helium-3 Bolometry Using Nanowire Resonators with SQUID Readout for the QUEST-DMC Experiment

E. Leason[1,2] · L. V. Levitin[2] · S. Autti[3] · E. Bloomfield[1] · A. Casey[2] · N. Darvishi[2] · N. Eng[2] · P. Franchini[1] · R. P. Haley[3] · P. J. Heikkinen[2] · A. Jennings[4] · A. Kemp[5] · J. March-Russell[1] · A. Mayer[3] · J. Monroe[1] · D. Muenstermann[3] · M. T. Noble[3] · J. R. Prance[3] · X. Rojas[2] · T. Salmon[3] · J. Saunders[2] · J. Smirnov[6] · R. Smith[1,2] · M. D. Thompson[3] · A. Thomson[3] · A. Ting[2] · V. Tsepelin[3] · S. M. West[2] · L. Whitehead[3] · D. E. Zmeev[3] · QUEST-DMC Collaboration

Received: 4 September 2025 / Accepted: 5 January 2026

Abstract
Superfluid helium-3 bolometers can be utilised for dark matter direct detection searches. The extremely low heat capacity of the B phase of the superfluid helium-3 at ultra-low temperatures offers the potential to reach world leading sensitivity to spin-dependent interactions of dark matter in the sub-GeV/c^2 mass range. Here, we describe the development of bolometry using both micron scale and sub-micron diameter vibrating wire resonators, with a SQUID amplifier-based readout scheme. Characterisation of the resonators and bolometer measurements are shown, including the use of nonlinear operation and the corresponding corrections. The bolometer contains two vibrating wire resonators, enabling heat injection calibration and simultaneous bolometer tracking measurements. Coincident events measured on both vibrating wire resonators verify their response. We also demonstrate proof of concept frequency multiplexed readout. Development of these measurement techniques lays the foundations for the use of superfluid helium-3 bolometers, instrumented with vibrating nanomechanical resonators, for future low-threshold dark matter searches.

Keywords Helium-3 · Dark matter · Nanomechanical resonators

1 Introduction

The QUEST-DMC programme uses a superfluid helium-3 bolometer for dark matter direct detection searches. This detection scheme, described in Ref. [1], offers low-energy threshold detection which is well suited to sub-GeV/c^2 dark matter masses

Extended author information available on the last page of the article

Published online: 07 February 2026

and has the potential to reach world leading sensitivity to dark matter interactions in this mass range [2, 3].

The bolometer measures production of thermal excitations in the form of quasiparticles, resulting from energy deposition in the superfluid target. This exploits the extremely low heat capacity of the B phase of superfluid helium-3 at ultra-low temperatures below 0.4 mK, where most quasiparticles are bound into Cooper pairs. Vibrating wire resonators are utilised primarily to measure the strongly temperature-dependent quasiparticle density and secondly as heaters for calibration. This technique was originally developed by the ULTIMA collaboration [4]. In QUEST-DMC, we expect several orders of magnitude improvement in sensitivity as a result of two key developments: novel vibrating wire resonators with sub-micron diameter and superconducting quantum interference device (SQUID) readout. Both are expected to significantly improve the bolometer resolution [1].

We demonstrate the reliable SQUID readout of the bolometer, with the readout scheme outlined in Sect. 3. Characterisation of the resonators and operation in the nonlinear regime close to the critical velocity is shown in Sect. 4. This section outlines the measurements necessary to correct for the nonlinear effects in the resonance width. In order to infer the energy deposit, a calibration is required. For this purpose, Sect. 6 shows the use of a second vibrating wire as a heater, with low-power heat injection reaching the energies of interest for the dark matter search. Having two vibrating wires also allows for simultaneous tracking measurements, as shown in Sect. 6.2. We measure coincident bolometer events on both wires, verifying their response. The energy calibration with low-energy gamma rays and a study of noise performance of the bolometer will be subject of a separate report.

Our circuit contains no additional cryogenic components apart from the vibrating wire and integrated SQUID current sensor [5], in comparison with more complex schemes developed previously [6, 7]. This simplicity lends itself to scaling up by running an array of bolometers in parallel. Furthermore, we demonstrate multiplexing in Sect. 6.3 by reading out two resonances with one SQUID simultaneously.

2 Experimental Set-up

The experimental assembly is illustrated in Fig. 1. A wet commercial dilution refrigerator was extended with a large copper nuclear demagnetisation stage. The bolometer is situated inside a mostly metallic cell filled with helium-3, mounted on top of the demagnetisation stage. Helium-3 in the main reservoir of roughly 2 cm^3 is cooled by a silver sinter heat exchanger of estimated surface area 20 m^2.

The superfluid helium-3 bolometer is a $7 \times 5 \times 5$ mm cuboid open to the main reservoir via a 0.3-mm-diameter orifice, which provides the cooling of the superfluid helium-3 target. A well-defined bolometer volume is essential to establishing a reliable energy calibration. To this end, the bolometer cavity was machined out of a solid copper puck, with the upper and lower walls constructed from flat copper foils. This essentially metallic construction ensures no heating of the bolometer due to heat release in disordered materials such as paper and epoxies, traditionally used in

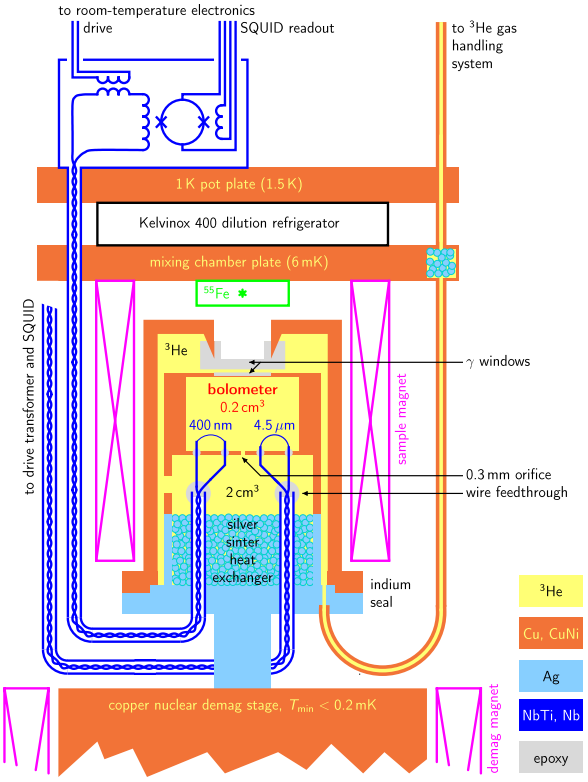

Fig. 1 Schematic drawing of the bolometer cell mounted on a nuclear demagnetisation refrigerator. The cell includes the silver sinter heat exchanger, reservoir of superfluid ^{3}He (2 cm^3) and bolometer opened to the reservoir via a small orifice. The base of the cell is in good thermal contact with the copper demagnetisation stage, precooled by an Oxford Instruments Kelvinox 400 dilution refrigerator (DR). The bolometer is equipped with thermometer/heater vibrating wires, connected to SQUID sensors with integrated drive transformers, mounted at the 1 K pot plate of DR. The magnetic fields for the operation of vibrating wires are provided by a small superconducting magnet, separate from the large demagnetisation magnet situated in the ^{4}He bath of the cryostat. The bolometer and cell walls include gamma ray transparent windows for energy calibration using a ^{55}Fe source located outside the cell

construction of helium-3 bolometers. Minimal amounts of Stycast 1266 and Araldite epoxies were used to seal the joints between the puck and foils and for the vibrating wire feedthroughs. The main materials used have been screened in the Boulby Underground Germanium Screening facility to ensure acceptable levels of radiopurity [8].

The bolometer contains NbTi vibrating wires of two diameters: the 4500 nm wires were obtained commercially as filaments of a multifilament superconducting cable in copper matrix; the 400 nm nanowires (Fig. 2) were produced by drawing such cable through a series of dies, similar to the procedure described in Ref. [9]. Sections of complete cable at both ends of the vibrating wires served as "legs" and were mounted in the bolometer wall using Araldite epoxy.

The vibrating wires are connected to SQUID current sensors, installed on the 1 K pot plate of the dilution refrigerator. Transformers integrated into the SQUIDs were used to drive the vibrating wires [5]. The electrical connections to the cell are minimal: a single NbTi twisted pair shielded inside a Nb tube per vibrating wire. This electrical circuit and its performance are discussed in Sect. 3.

The magnetic field for electrical excitation and readout of the mechanical resonators is provided by a small superconducting magnet suspended off the mixing chamber plate of the dilution refrigerator. The nuclear stage is also rigidly attached

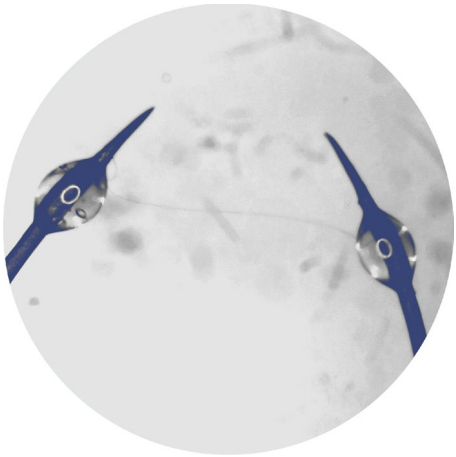

Fig. 2 A 400 nm nanowire photographed through an optical microscope. Araldite epoxy beads stabilises the extruded superconducting cable at both ends of the wire. In the section between the beads, all filaments but one were removed after etching away the copper matrix

to this plate, minimising relative motion of the bolometer and the magnet. In the earlier Lancaster-style design [1], the bolometer is embedded inside an assembly of sintered nuclear stages, to reach exceptionally low helium temperatures. In contrast, here we can alter the sample field independent of the demagnetisation field, in order to investigate the performance of the SQUID readout.

In addition to direct heat injection, our approach to energy calibration will use low-energy deposition from a well-characterised ^{55}Fe source. The standard packaging of commercial radioactive sources is too bulky to incorporate these inside the cell; thus, the cell and bolometer walls have windows with reduced gamma photon attenuation. Our ^{55}Fe source has a low nominal activity ensuring no prohibitive heat release in any part of the set-up and making the handling of the source safe. The 1-mm-thick Stycast 1266 epoxy window in the cell lid and 5 µm copper foil window in the bolometer were selected to have sufficient strength and appropriate gamma attenuation.

Important properties of the superfluid helium-3 target can be tuned with pressure [10]; therefore, we designed the cell capable to withstand tens of bars. The wire feedthroughs and the outer gamma window are positioned on the inside of the cell, so that the helium under pressure squeezes epoxy around metal tubes. The cell has been successfully leak tested up to 20 bar. While the pressure inside the bolometer is normally the same as in the main reservoir, transient pressure gradients are unavoidable when loading or emptying the cell. To prevent deformation or damage to the 5 µm copper window in the bolometer wall, this was reinforced with a $\sim 100\,\mu$m film of Stycast 1266 with negligible gamma attenuation.

All measurements presented in this paper were obtained at a cell pressure of 18.5 bar, stabilised to 1 mbar using a quartz pressure transducer and a heated gas volume operated by a proportional–integral controller. At this pressure, the superfluid transition is at $T_c = 2.2$ mK and the lowest temperature reached in the bolometer was $0.135\,T_c$.

3 SQUID Readout Scheme

The scheme for reading out the voltage-driven vibrating wire, using a two-stage SQUID current sensor [5], is shown in Fig. 3. Voltage $V_x = 2i\pi f M_x I_x$ is applied inductively by driving the current I_x at frequency f, via the transformer with mutual inductance M_x. This current is generated by a voltage oscillator via a resistor $R_x = 1$–100 kΩ. The SQUID detects the current I_i flowing through the loop comprised of the wire of impedance Z, SQUID input coil of inductance L_i (including inductance of the twisted pair between the wire and the SQUID, and self-inductance of the secondary of the drive transformer) and series resistance R of the contacts/wire,

$$I_i = \frac{V_x}{Z_\Sigma} = \frac{V_x}{Z + R + 2i\pi f L_i}. \tag{1}$$

Here, $Z_\Sigma = Z + R + 2i\pi f L_i$ is the total impedance of the loop. This gives flux $\phi = M_i I_i$ in the SQUID, which is read out using flux-locked loop electronics [11]. Note that all alternating currents, voltages, forces, velocities and powers are rms throughout.

We infer I_i from the real and imaginary components, X and Y, of the voltage measured by the lock-in at the output of the flux-locked loop,

$$I_i = \frac{X + iY}{(R_f/M_f) \times M_i}. \tag{2}$$

Here, R_f is resistance of the feedback resistor, M_f is the mutual inductance between the feedback coil and the SQUID, and M_i is the mutual inductance between the input coil and the SQUID. This is used to calculate the impedance of the wire,

$$Z = \frac{2i\pi f M_x}{I_i/I_x} - R - 2i\pi f L_i. \tag{3}$$

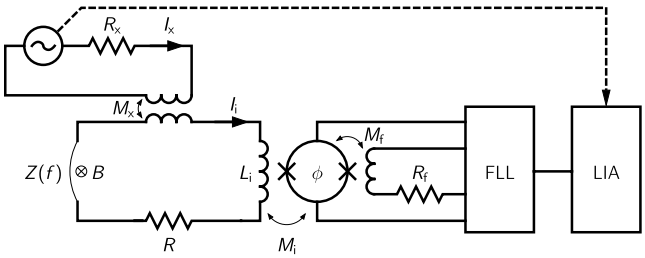

Fig. 3 SQUID readout circuit. The vibrating wire forms part of an input loop of a SQUID current sensor together with contact resistance R, input coil L_i of the SQUID and drive transformer with mutual inductance M_x. The wire is excited by voltage V_x, applied by driving a current, I_x, via the transformer with mutual inductance M_x. The SQUID operated in flux-locked loop (FLL) detects the current I_i in the loop. The FLL gain is determined by R_f and M_f. A phase-sensitive lock-in amplifier (LIA) detects the component of I_i at the frequency of the drive

3.1 Broad Frequency Sweeps

The propagation of the signal through the measurement circuit leads to a correction that we model by,

$$I_{\mathrm{i}} \to \left(1 - \frac{if_{\mathrm{c}}}{f}\right) \exp\left(-ia - ibf\right) I_{\mathrm{i}}. \tag{4}$$

Here, the first term describes the AC input coupling of the lock-in, which acts as a first-order high-pass filter with cut-off frequency $f_{\mathrm{c}} = 80$ Hz. The second term represents the rest of the circuit, where a simple phenomenological expression $a + bf$ for the phase shift proves adequate. This correction is applied to the measured I_{i} prior to evaluation of the impedance according to Eq. (3).

The values of a and b as well as circuit parameters R and L_{i} are obtained from broad (5 Hz–10 kHz) frequency sweeps carried out at zero magnetic field, where there is no contribution to the total impedance of the SQUID input loop from the vibrating wire resonators, and the data can be fitted to Eq. (3) with $Z = 0$. The fit was verified by checking that $\mathrm{Im}\, Z_{\Sigma}(f)$ is a straight line with zero intercept. The procedure was repeated when changes were made to the resistors in the SQUID readout circuit.

4 Resonator Characterisation

4.1 Narrow Frequency Sweeps

In order to characterise the vibrating wire resonances, narrow frequency sweeps were carried out at constant I_{x} in a range of magnetic fields, illustrated in Fig. 4. The impedance obtained from Eq. (3) was fitted to a Lorentzian,

$$Z(f) = \frac{ifA}{f_0^2 - f^2 + if\Delta f}, \tag{5}$$

with resonance amplitude A and resonance frequency f_0. The resonance width Δf includes contributions from both the intrinsic (as observed in vacuum) and quasiparticle damping. The latter is a direct measure of the bolometer temperature, enabling the tracking measurements described in Sect. 5.

In the simple approximation of a rigid beam moving rectilinearly perpendicular to the magnetic field, the resonance amplitude $A = \ell B^2 / 2\pi m$ can be parametrised by effective length ℓ and mass per unit length m of the vibrating wire [7]. We find

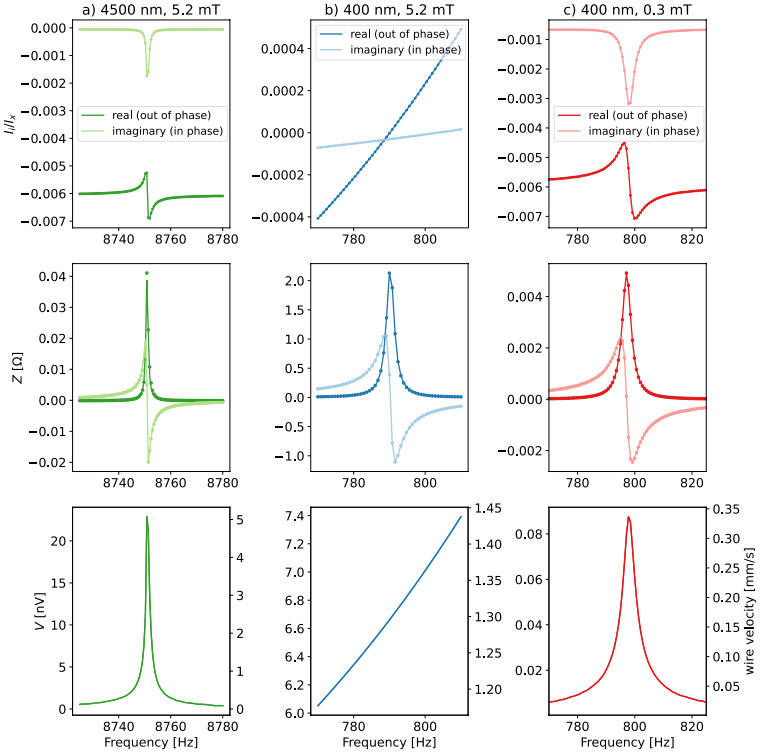

Fig. 4 Frequency sweeps for the **a** 4500 nm nanowire at 5.2 mT field, **b** 400 nm wire at 5.2 mT field and **c** 400 nm at 0.3 mT—in all cases at 18.5 bar and 0.27 mK. The top panel shows the ratio of measured current to drive current and resonance-like behaviour depends on the relationship between them. The middle panel shows the impedance of the wire. The lower panel shows the derived voltage across the wire and estimated velocity of the wire. The strong field dependence of the wire impedance $Z \propto B^2$ manifests in very different shape of the raw data $I_i(f)/I_x$ and hence $v(f)$ for the same wire at fields where $Z(f_0) \gg 2\pi f_0 L_i$ (**b**) and $Z(f_0) \approx 2\pi f_0 L_i$ (**c**)

$\ell = 1.0$ mm for the 1.4-mm-long 400 nm nanowire and $\ell = 0.9$ mm for the 1.9-mm-long 4500 nm wire. The discrepancy between ℓ and the actual wire length, more pronounced for the arched 4500 nm wire, arises from the distribution of velocity and displacement along the wire.

Extracting ℓ from A enables us to estimate the velocity,

$$v = \frac{|V|}{\ell B} = \frac{|ZI_i|}{\ell B}, \tag{6}$$

from the voltage V across the wire, also shown in Fig. 4. Note that the raw data $I_i(f)/I_x$ look drastically different depending on the relative scale of the on-resonance wire impedance $Z(f_0)$ and the impedance of the input coil of the SQUID $2i\pi f_0 L_i$. Consequently, in the $Z(f_0) \ll 2\pi f_0 L_i$ regime the wire velocity is nearly constant when sweeping the resonance (Fig. 4b), while at $Z(f_0) \gtrsim 2\pi f_0 L_i$ there is a well-pronounced velocity maximum at a frequency where $\mathrm{Im}\, Z(f) + 2i\pi f_0 L_i = 0$ (Fig. 4a,c).

4.2 Drive Amplitude Sweeps

The velocity dependence of the wire response can be characterised with drive amplitude sweeps at a fixed frequency, typically on resonance. To a geometrical factor of order unity, we estimate the force on the wire as,

$$F = |I_i \ell B|. \tag{7}$$

On-resonance drive sweeps on 400 nm nanowire are shown in Fig. 5. When oscillating at small velocities the response of the wire is linear, with a linear damping force $F_d \propto v$. However, as velocity increases beyond a few mm/s the damping becomes nonlinear. The onset of the nonlinearity is expected around $v = k_B T/p_F \simeq 4$ mm/s [12].

As velocity is increased further, emission of bound quasiparticles into the bulk superfluid leads to an increase in dissipation [13, 14], giving a sharp rise in $F_d(v)$ observed at $v = 32$ mm/s, of order Landau critical velocity $v_L = \Delta/p_F \simeq 60$ mm/s. For a macroscopic wire of circular cross section with diameter d much greater than the coherence length $\xi_0 = 22$ nm (at 18.5 bar), this phenomenon is predicted to onset at rms velocity $v_L/3\sqrt{2} = 14$ mm/s. Here, the discrepancy may reflect neglecting the velocity distribution along the wire in Eq. (6) and/or the mesoscopic character ($d \sim 10\,\xi_0$) of the 400 nm nanowire.

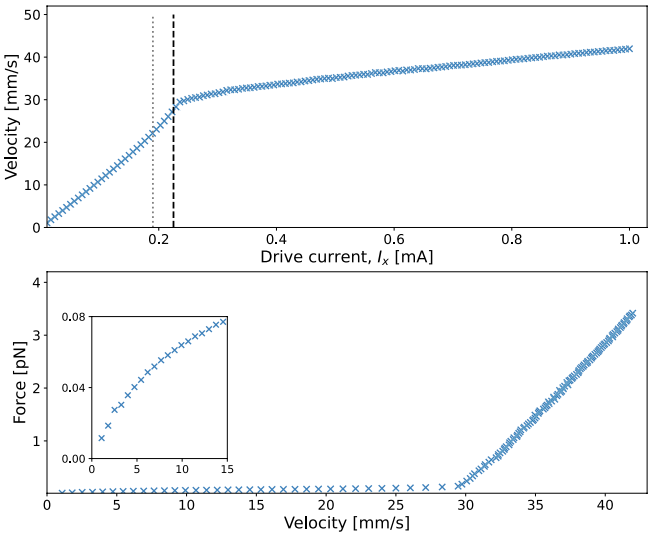

Fig. 5 Drive amplitude sweep for the 400 nm nanowire at the resonant frequency of 799 Hz. Upper plot shows rms velocity versus drive current, with dotted grey and dashed black lines indicating the selected tracking drive and critical velocity, respectively. Lower plot shows the corresponding drive force vs velocity, demonstrating characteristic regions of quasiparticle injection and nonlinearity

4.3 Nonlinearity Correction

The operating velocity is below the critical velocity, but above the linear response regime. The nonlinearity manifests via a velocity-dependent resonance width $\Delta f(v)$ and can be taken into account following Ref. [15]. From Eq. (5), this width can be obtained as,

$$\Delta f(v) = \mathrm{Re}\left(\frac{A}{Z(f,v)}\right), \tag{8}$$

from a single impedance measurement $Z(f, v)$ at a frequency f and velocity v. The resonance amplitude A is determined by fitting Eq. (5) to a low-drive frequency sweep, typically at sub-mm/s velocity. In principle, Eq. (8) is valid at any measurement frequency, but practically the high-resolution determination of $\Delta f(v)$ is limited to the vicinity of the resonance where Z is predominantly real.

The measured width can be written as the sum of intrinsic and quasiparticle damping terms,

$$\Delta f(v) = \Delta f_\mathrm{i} + \Delta f_0 S(\gamma v/v_0). \tag{9}$$

Here, the intrinsic damping is characterised by the width $\Delta f_\mathrm{i} = 0.15$ Hz measured for both resonators in vacuum prior to filling the cell with helium-3. The second term is the width due to quasiparticle damping only. Following Ref. [15], we express it as a product of the width Δf_0 at $v \to 0$ and a correction factor,

$$S(c) = \frac{2}{c}\left(I_1(c) - L_{-1}(c) + \frac{2}{\pi}\right), \tag{10}$$

determined by the reduced velocity $c = \gamma v/v_0$. Here, γ is a dimensionless adjustable parameter of order unity that encodes the velocity profile, I_1 is the modified Bessel function of the first kind of order 1 and L_{-1} is the modified Struve function of order -1. Thus, we extract $\Delta f_0 = \left(\Delta f(v) - \Delta f_\mathrm{i}\right)/S(\gamma v/v_0)$, simplifying further analysis of the bolometer response. The performance of this correction procedure up to velocities of tens of mm/s is illustrated in Fig. 6. Here we note again that the 400 nm oscillator is mesoscopic ($d \gg \xi_0$ does not hold); therefore, departures from Eqs. (9, 10) are expected [16]. To improve the nonlinearity correction the distribution of velocity along the wire can be considered, this will be the subject of future work.

5 Bolometer Measurements

To operate the cell as a bolometer, the resonator is interrogated at the resonant frequency and a constant drive level, below the onset of pair breaking and low enough for the nonlinearity correction to work, see Sects. 4.2 and 4.3. From the measured wire impedance Z, we obtain the resonance width Δf_0 (corrected for finite velocity and intrinsic damping) according to Eqs. (8)–(10). This procedure takes the

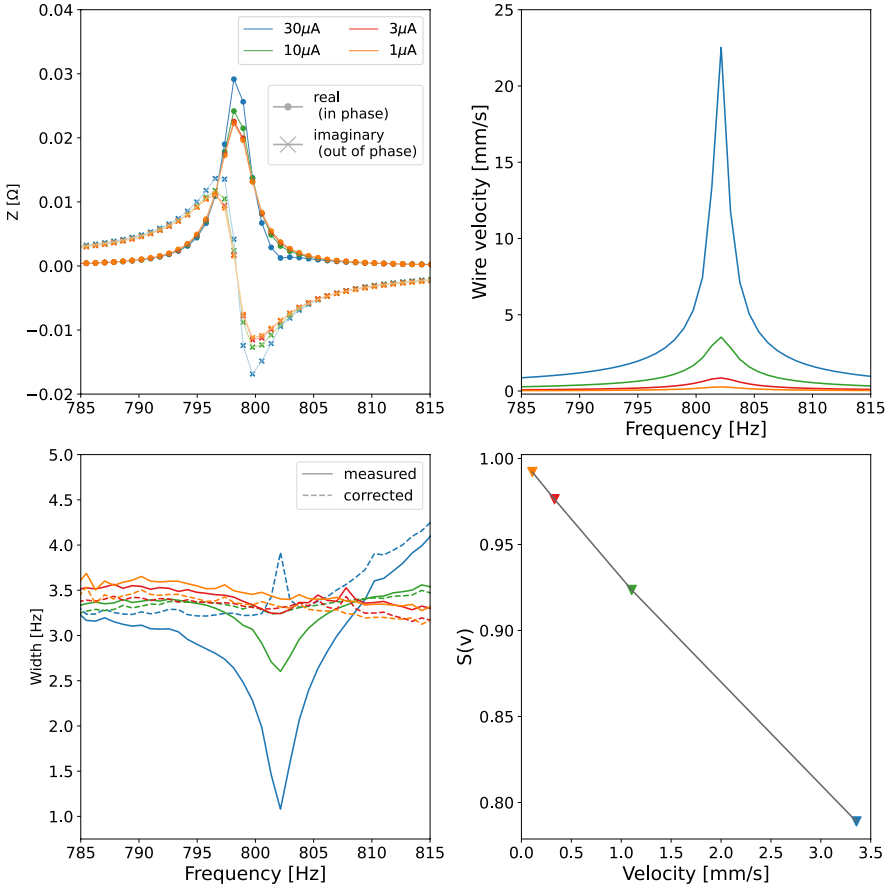

Fig. 6 Demonstration of the nonlinearity correction for the 400 nm nanowire. Upper left: frequency sweeps at different values of drive current I_x. Upper right: corresponding velocity across the sweep. Lower left: width inferred from Eq. (8) before and after correction to the linear regime using Eq. (9). Lower right: correction factor $S(v)$ as a function of velocity, the triangles represent the correction applied on resonance

resonance amplitude A as an input parameter, so the tracking is paused every few hours for low-drive frequency sweeps. The conversion of width to temperature is based on Ref. [17].

Figure 7 illustrates tracking measurements. The bolometer response to a heating event at t_0 can be described as a function of time,

$$\Delta f_0(t) = \Delta f_0^{\text{base}} + \Theta(t - t_0) H \frac{\tau_b}{\tau_b - \tau_w} \left[\exp\left(\frac{t_0 - t}{\tau_b} \right) - \exp\left(\frac{t_0 - t}{\tau_w} \right) \right], \quad (11)$$

where Δf_0^{base} is the baseline width, $\Theta(t)$ is the Heaviside step function and H is the maximum (instantaneous) increase in width corrected for the response time of the bolometer [4]. Two time constants determine the pulse shape, the bolometer time

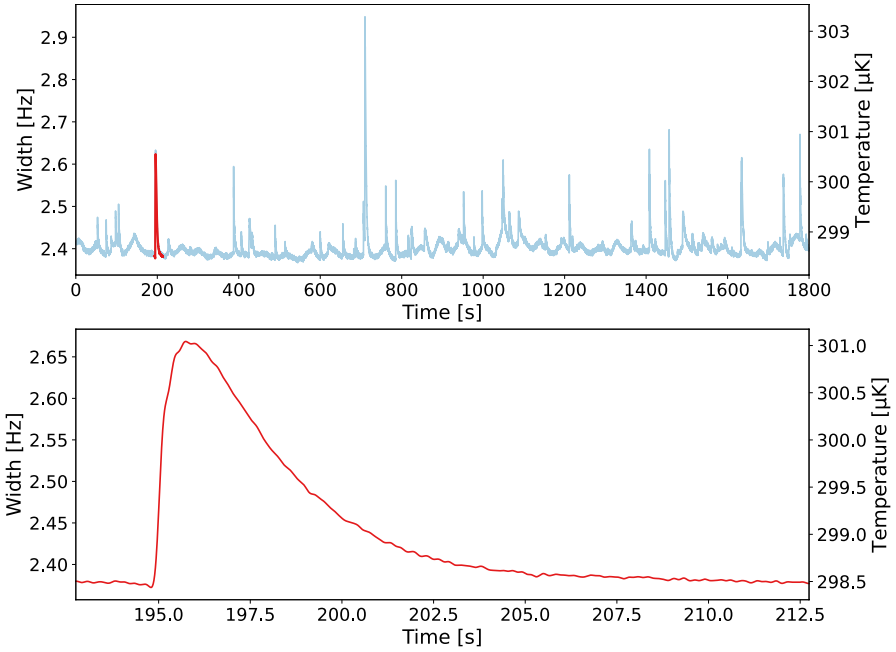

Fig. 7 Example tracking data from 400 nm nanowire, driven on resonance in a 5.2 mT field at 0.3 mK. Example bolometer pulse shape shown in the lower panel

constant τ_b and the wire time constant τ_w. These four parameters are determined by fitting the pulses found in the tracking mode data. The amplitude H reflects the magnitude of heating (or energy) causing the event. The baseline width Δf_0^{base} and wire time constant $\tau_w \approx 1/\pi\Delta f_0^{\text{base}}$ depend on bolometer temperature for a given dataset. The bolometer time constant τ_b depends on the bolometer geometry and remains constant across all datasets for a given bolometer.

Most of the instantaneous heating events in the bolometer result from particles such as cosmic rays or radioactive decay products interacting with the superfluid helium [1, 8]. An example bolometer pulse is shown in Fig. 7 and large pulses such as this one most likely originate from cosmic ray interactions.

6 Two-Wire Operation

6.1 Heat Injection Calibration

The bolometric technique relies on conversion of the resonance width change, observed in the tracking measurements, to temperature change or energy. Width of the resonance is proportional to the damping force, F_d, from momentum transfer in quasiparticle collisions with the wire [18],

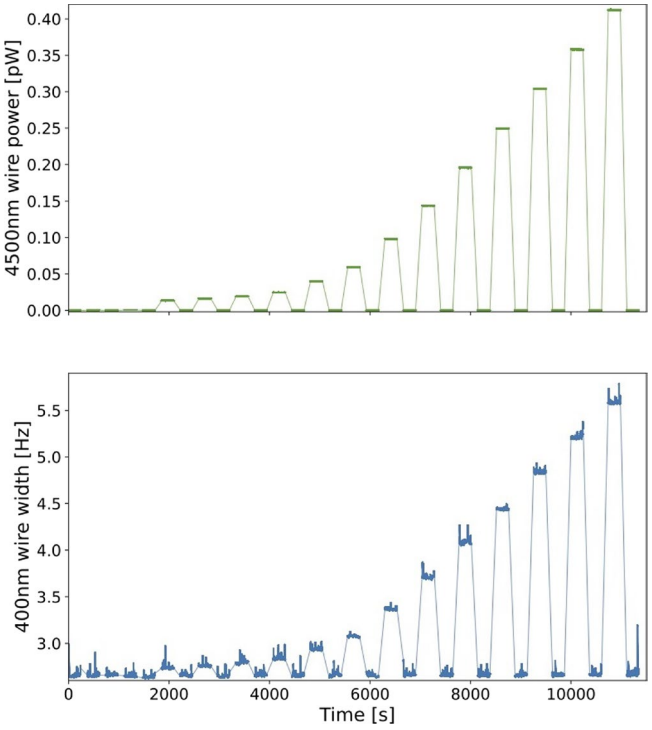

Fig. 8 Stepped heat injection using the 4500 nm wire driven above critical velocity (upper) and the measured width response of the 400 nm nanowire (lower)

$$\Delta f_0 = \alpha \frac{F_\mathrm{d}}{2\pi m v} = \gamma' \frac{dp_\mathrm{F}^2 \langle n v_\mathrm{g} \rangle}{2\pi m k_\mathrm{B} T} = \gamma' \frac{8 dp_\mathrm{F}^4}{mh^3} \exp(-\Delta / k_\mathrm{B} T). \tag{12}$$

Here, d is the wire diameter, p_F is the Fermi momentum, $\langle n v_\mathrm{g} \rangle$ is the density of quasiparticle or quasihole excitations n multiplied by the appropriate group velocity v_g and Δ is the superfluid gap at the operating temperature and pressure. Dimensionless constants α and γ' depend on wire geometry and details of the scattering process. This enables conversion of measured widths to temperature and energy, once bolometer calibration has determined the value of γ'. One calibration method, demonstrated in Refs. [4, 18, 19], is to inject heat into the system by mechanical dissipation.

For heat injection over timescales longer than the bolometer time constant the bolometer will reach thermal equilibrium as a result of quasiparticle–wall and quasiparticle–quasiparticle collisions. This means the number density of quasiparticles will quickly become constant and resonance width reaches a new stable value. In this state, the total power entering the bolometer, from both the heater and wall heat leaks, must balance power carried by the quasiparticles

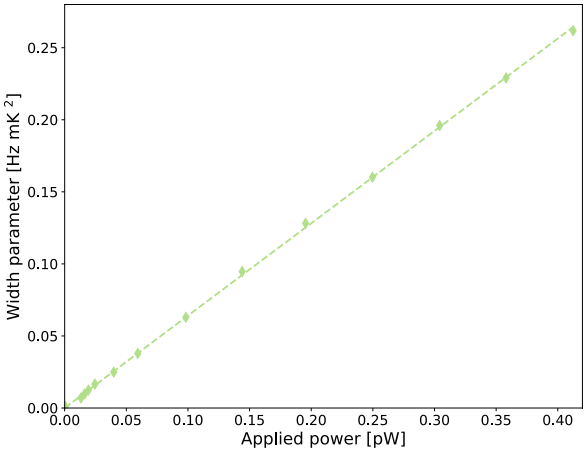

Fig. 9 Linear relationship between power injected by the 4500 nm wire and width parameter measured using the 400 nm nanowire

leaving the orifice, $\dot{Q}_\mathrm{T} = \dot{Q}_\mathrm{h} + \dot{Q}_\mathrm{w} = \dot{Q}_o$. The power transmitted out through the orifice can be written as [18],

$$\dot{Q}_o = \frac{\langle n v_\mathrm{g} \rangle}{4} \langle E \rangle A_\mathrm{o}. \tag{13}$$

Here, $\langle E \rangle$ is the average quasiparticle energy and A_o is the effective area of the orifice. This can be determined from the bolometer time constant $\tau_\mathrm{b} = 4V_\mathrm{b}/A_\mathrm{o}\langle v_g \rangle$ for bolometer volume V_b and mean quasiparticle group velocity $\langle v_\mathrm{g} \rangle \approx \sqrt{k_\mathrm{B}T/\Delta v_\mathrm{F}}$. Combining with Eq. (12), the width can be related to total power,

$$\Delta f_0 T \langle E \rangle = \gamma' \frac{2dp_\mathrm{F}^2}{\pi k_\mathrm{B} m A_\mathrm{o}} \dot{Q}_\mathrm{T}. \tag{14}$$

Subtracting input power from the walls using the bolometer base width, Δf_0^base, and substituting $\langle E \rangle = \Delta + k_\mathrm{B}T$ allow us to define the width parameter [19],

$$W_\mathrm{p} = (\Delta f_0 - \Delta f_0^\mathrm{base}) T \left(\frac{\Delta}{k_\mathrm{B}} + T \right). \tag{15}$$

This absorbs the temperature dependence of $\langle E \rangle$ in Eq. (14) such that the bolometer response can be related to applied heater power,

$$W_\mathrm{p} = \gamma' \frac{2dp_\mathrm{F}^2}{\pi k_\mathrm{B} m A_\mathrm{o}} \dot{Q}_\mathrm{h}. \tag{16}$$

The calibration constant γ' can be determined from the steady-state response $\Delta f_0(\dot{Q}_\mathrm{h})$, as shown in Fig. 8. Periods of zero applied power were inserted between each period of constant heating, in order to correct for any temporal variations in Δf_0^base. The 4-min wait at each power, much longer than τ_b, ensures the equilibrium. Even though the 4500 nm wire as a heater operates in a nonlinear regime, the

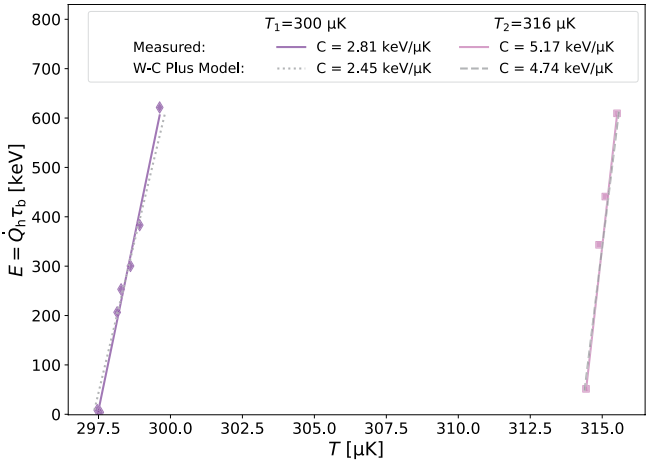

Fig. 10 Energy versus bolometer temperature obtained from the data shown in Fig. 8 and similar measurement at higher temperatures. We compare the heat capacity C derived from a straight line fit to each dataset to the prediction of the "weak coupling plus" theory [17, 20] for 0.17 cm^3 of the B phase at 18.5 bar

detected current $I_i(t)$ in time domain is nearly sinusoidal. Therefore, we derive the power applied using the wire as $\dot{Q}_h = |I_i|^2 \, \mathrm{Re}(Z)$.

Bolometer tracking data taken during each of these 4-min periods was used to measure the width parameter, defined in Eq. (15). These periods also contained background events, similar to those seen in Fig. 7, so the mean width parameter was calculated using the quiet periods of data which did not contain any heating pulses. Figure 9 shows the linear response of the measured width parameter on the 400 nm nanowire to injected power, which validates our model and assumption of thermal equilibrium in the bolometer. The linear fit was consistent for different 400 nm drive amplitudes and tracking measurements times. Once the calibration constant has been extracted from this fit, Eq. (12) can be used to find energy of individual pulse events using either the measured pulse amplitude or area.

The increase in bolometer temperature in response to the steady-state applied power $\dot{Q}_h$ is equivalent to a transient response to a heat pulse $E = \dot{Q}_h \tau_b$, where the steady-state power is integrated over the bolometer time constant τ_b. Thus, from the heater calibration measurements, we obtain the bolometer heat capacity $C = d(\dot{Q}_h \tau_b)/dT$. Figure 10 shows that this measured heat capacity is in good agreement with the heat capacity of the superfluid B phase, calculated [17] using the value of the energy gap Δ given by the "weak coupling plus" theory [20]. The deviations may stem from a small error in the value of Δ we use or reflect the additional heat capacity of solid helium and Andreev surface-bound states on the bolometer walls [21].

6.2 Simultaneous Tracking

Tracking data were acquired on both wires simultaneously, at 2.6 mT field and 0.3 mK bolometer temperature. A lower field was used here to access the critical velocity of the 400 nm wire, since the velocity peak is offset from the resonance occurring at the field-dependent impedance minimum. This measurement involved driving both wires simultaneously at their resonance frequency and acquiring bolometer tracking data, using the procedure outlined in Sect. 5, for both wires at the same time. Since the bolometer slowly warms up after a demagnetisation, the tracking measurements were periodically paused for (1) low-drive frequency sweeps to recalibrate resonance amplitude A and (2) heater calibrations.

In this dataset, simultaneous heating events can be observed on the two wires. Figure 11 shows an example of simultaneous pulses, fit with the expected bolometer heating pulse shape from Eq. (11). Here, higher baseline noise is seen in the 4500 nm tracking data due to the lower field. The pulse shape fits for this dataset show consistent bolometer time constant of 3 s for both wires and rise times of 0.2 s and 0.6 s for the 400 nm and 4500 nm wire, respectively. There was a factor of 10 difference observed in the width change for the two wires. This is roughly consistent with the ratio of the wire diameters; however, it may not be exact due to mesoscopic character of the thinner wire. This effect demonstrates the benefits

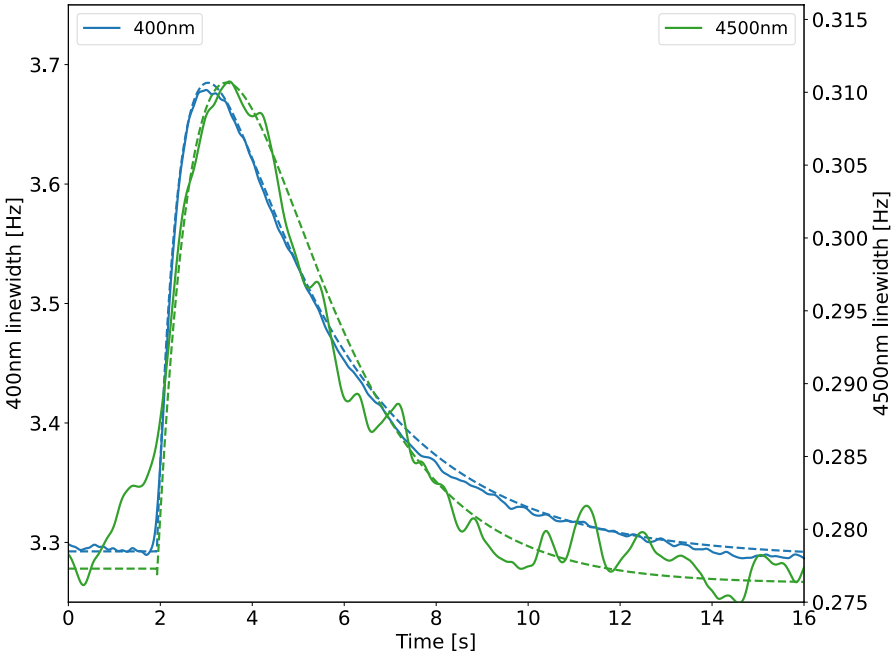

Fig. 11 Coincident bolometer pulses observed when tracking on both wires simultaneously, solid line shows data and dashed line shows the fit to Eq. (11)

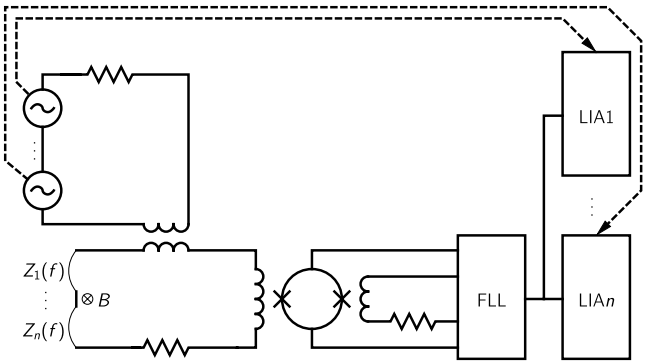

Fig. 12 Circuit diagram for readout of multiple vibrating wires with one SQUID sensor. All vibrating wires represented by the impedances $Z_1(f)$, ..., $Z_n(f)$ must resonate at sufficiently different frequencies. A single multichannel lock-in amplifier can drive and detect multiple resonances simultaneously

of sub-micron wires: faster bolometer rise and lower temperature, where the width is dominated by intrinsic damping [1].

6.3 Multiplexing

Figure 12 shows how several vibrating wires can be simultaneously read out by a single SQUID sensor. Provided the resonances are sufficiently separated in frequency ($|f_0^A - f_0^B| \gg \Delta f^A + \Delta f^B$ for wires A and B, higher harmonics must also be separated), the wires make negligible contributions to the total impedance of the input loop near each other's resonance. Here, we demonstrate this concept, in a different bolometer, using a 400 nm nanowire, that exhibits an additional low-frequency vibrational mode due to fabrication/mounting issues. This wire has a main mechanical resonance at 1170.9 Hz and an additional resonance, with much lower amplitude, at 814.6 Hz. Figure 13(a) shows frequency sweeps across both resonances, with and without a simultaneous drive applied to the other resonance. Low drive amplitudes were chosen to ensure no significant coupling between the modes due to nonlinear effects, allowing independent bolometer tracking measurements at both resonances. The simultaneous readout of the two vibrational modes with a single SQUID is illustrated in Fig. 13(b). This proof of concept demonstrates than the readout scheme can reliably track multiple frequencies, which can be engineered to be well separated for different vibrating wires using geometry or mounting stress.

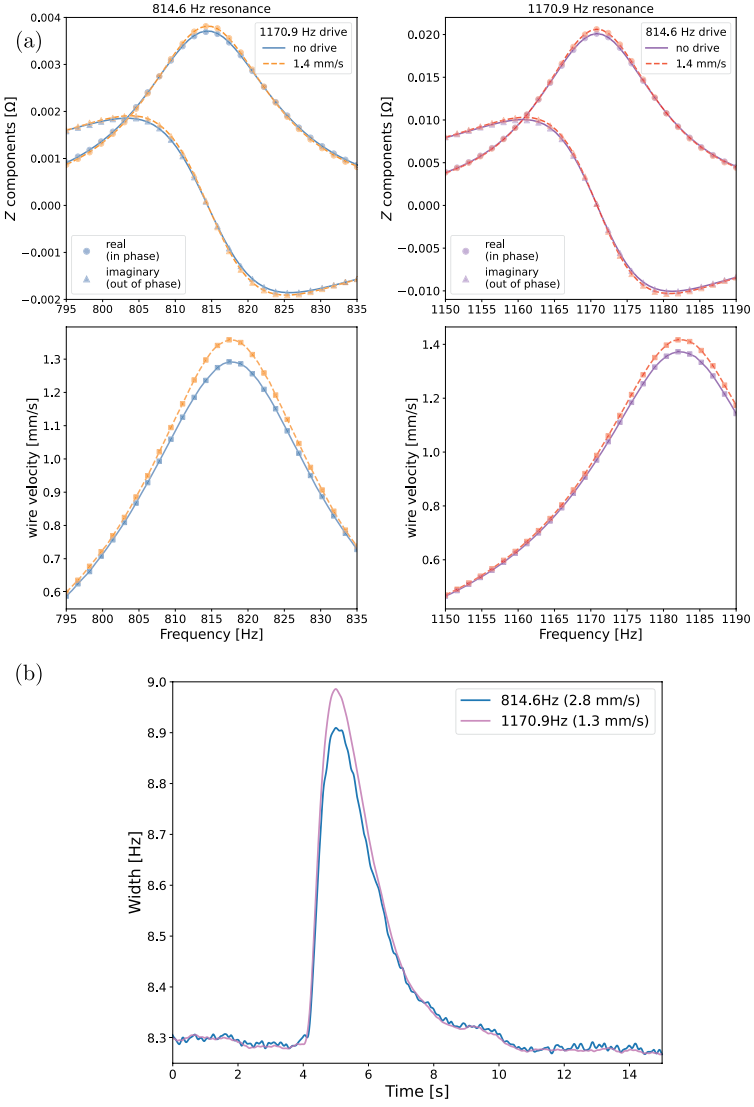

Fig. 13 Measurements of two frequency modes using the multiplexed readout scheme. **a** Narrow frequency sweeps on two modes of the same 400 nm nanowire, in both the absence and presence of drive on the other mode, with velocity of the second mode indicated in the legend. **b** Bolometer pulse measured with simultaneous tracking measurements on both modes, with velocity of each mode indicated in the legend

7 Conclusions and Outlook

We have demonstrated the operation of a superfluid helium-3 bolometer at sub-millikelvin temperatures, using nanomechanical resonators with SQUID readout. Using a second wire for calibration in this scheme allows for injection of much

lower heat power than has been done previously, reaching the energy region of interest for a low-mass particle dark matter search.

This lays the foundation for detection of energy deposits from particle interactions in the superfluid, forming the basis of a dark matter direct detection search. The next development will be a comparison of energy deposits from particle calibration sources with the energy injection using a heater wire, together with characterisation and optimisation of the energy resolution. This will inform the energy partition model used in the dark matter search analysis outlined in Ref. [1]. Previous energy calibration measurements were taken in Lancaster [22] and later by the ULTIMA collaboration, as reported in Ref. [4, 23]. We aim to compare with these heating measurements, in particular the dependence on source particle type and energy. Further studies will also focus on detailed understanding of the noise performance and its relation to the resonator geometry. The resonator design will be optimised for minimising energy threshold, reliability and multiplexing. Ultimately the resonator characterisation, bolometer calibration and tracking measurements described here will be optimised for a low-threshold dark matter search and utilised to perform this over a long exposure.

Acknowledgements We thank Paul Bamford, Richard Elsom, Ian Higgs and Harpal Sandhu for excellent technical support.

Author Contributions The manuscript was written by EL and LL with contributions from all authors. The vibrating wire resonator fabrication was performed by DEZ. All data taking and analysis was carried out by EL and LL. All authors contributed to the project conceptualisation, design and data interpretation.

Funding This work was funded by UKRI EPSRC and STFC (Grants ST/T006773/1, ST/Y004434/1, EP/P024203/1, EP/W015730/1 and EP/W028417/1), as well as the European Union's Horizon 2020 Research and Innovation Programme under Grant Agreement no 824109 (European Microkelvin Platform). S.A. acknowledges financial support from the Jenny and Antti Wihuri Foundation. M.D.T acknowledges financial support from the Royal Academy of Engineering (RF/201819/18/2). J.Sm. acknowledges support from the UK Research and Innovation Future Leader Fellowship MR/Y018656/1. A.K. acknowledges support from the UK Research and Innovation Future Leader Fellowship MR/Y019032/1.

Data Availability No datasets were generated or analysed during the current study.

Declarations

Conflict of interest The authors declare no conflict of interest.

References

1. S. Autti, et al., QUEST-DMC superfluid helium-3 detector for sub-GeV dark matter. Eur. Phys. J. C **84** (2024). https://doi.org/10.1140/epjc/s10052-024-12410-8
2. N. Darvishi et al., Dark matter attenuation effects: sensitivity ceilings for spin-dependent and spin-independent interactions. J. Cosm. Astropart. Phys. **2025**, 017 (2025). https://doi.org/10.1088/1475-7516/2025/04/017
3. N. Darvishi et al., Dark matter eft landscape probed by quest-dmc. J. Cosm. Astropart. Phys. **2025**, 044 (2025). https://doi.org/10.1088/1475-7516/2025/10/044
4. C. Winkelmann et al., Bolometric calibration of a superfluid ^{3}He detector for dark matter search: direct measurement of the scintillated energy fraction for neutron, electron and muon events. Nucl. Instrum. Methods Phys. Res. A. **574**, 264–271 (2007). https://doi.org/10.1016/j.nima.2007.01.180
5. D. Drung et al., Highly sensitive and easy-to-use SQUID sensors. IEEE Trans. Appl. Supercond. **17**, 699–704 (2007)
6. D.I. Bradley, W.M. Hayes, An rf-squid amplifier system for use with vibrating wire resonators. J. Low Temp. Phys. **119**, 703–713 (2000). https://doi.org/10.1023/A:1004689830846
7. J. Martikainen, J.T. Tuoriniemi, SQUID amplifier system for vibrating wire resonators. J. Low Temp. Phys. **124**, 367–382 (2001). https://doi.org/10.1023/A:1017554708219
8. E. Leason et al., QUEST-DMC: background modelling and resulting heat deposit for a superfluid helium-3 bolometer. J. Low Temp. Phys. **215**, 465–476 (2024). https://doi.org/10.1007/s10909-024-03142-w
9. S. Autti, et al., Long nanomechanical resonators with circular cross-section (2023). https://arxiv.org/abs/2311.02452. arXiv:2311.02452
10. D. Vollhardt, P. Wölfle, *The Superfluid Phases of Helium 3* (Dover Publications, New York, 2013)
11. D. Drung, C. Hinnrichs, H. Barthelmess, Low-noise ultra-high-speed dc SQUID readout electronics. Supercond. Sci. Technol. **19**, S235–S241 (2006)
12. S.N. Fisher, A.M. Guénault, C.J. Kennedy, G.R. Pickett, Beyond the two-fluid model: transition from linear behavior to a velocity-independent force on a moving object in ^{3}He-B. Phys. Rev. Lett. **63**, 2566–2569 (1989). https://doi.org/10.1103/PhysRevLett.63.2566
13. S. Autti et al., Fundamental dissipation due to bound fermions in the zero-temperature limit. Nat. Commun. (2020). https://doi.org/10.1038/s41467-020-18499-1
14. S. Autti et al., Transport of bound quasiparticle states in a two-dimensional boundary superfluid. Nat. Commun. (2023). https://doi.org/10.1038/s41467-023-42520-y
15. V.V. Zavjalov, Using vibrating wire in non-linear regime as a thermometer in superfluid ^{3}He-B (2023). https://arxiv.org/abs/2303.01189. arXiv:2303.01189
16. S. Autti et al., Drag on cylinders moving in superfluid ^{3}He-B as the dimension spans the coherence length. J. Low Temp. Phys. **217**, 264–278 (2024). https://doi.org/10.1007/s10909-024-03165-3
17. V. Zavjalov, he3lib. https://github.com/slazav/he3lib (2024)
18. C. Bäuerle, Y.M. Bunkov, S.N. Fisher, H. Godfrin, Temperature scale and heat capacity of superfluid ^{3}He-B in the 100μK range. Phys. Rev. B **57**, 14381–14386 (1998). https://doi.org/10.1103/PhysRevB.57.14381
19. S.N. Fisher, A.M. Guénault, C.J. Kennedy, G.R. Pickett, Blackbody source and detector of ballistic quasiparticles in ^{3}He-B: emission angle from a wire moving at supercritical velocity. Phys. Rev. Lett. **69**, 1073–1076 (1992). https://doi.org/10.1103/PhysRevLett.69.1073
20. J. Serene, D. Rainer, The quasiclassical approach to superfluid ^{3}He-B. Phys. Rep. **101**, 221–311 (1983) https://www.sciencedirect.com/science/article/pii/0370157383900510
21. Y.M. Bunkov, R.R. Gazizulin, Direct observation of the specific heat of majorana quasiparticles in superfluid ^{3}He-B. Sci. Rep. **10**, 20120 (2020). https://doi.org/10.1038/s41598-020-77128-5
22. D. Bradley, M. Follows, W. Hayes, T. Sloan, The detection of low energy neutrons and γ-rays by superfluid ^{3}He, a potential dark matter detector. Nucl. Instrum. Methods Phys. Res. A. **370**, 141–143 (1996)
23. E. Moulin et al., Low-energy conversion electron detection in superfluid ^{3}he at ultra-low temperature. Nucl. Instrum. Methods Phys. Res. A. **548**, 411–417 (2005) https://www.sciencedirect.com/science/article/pii/S0168900205010521

Authors and Affiliations

E. Leason[1,2] · L. V. Levitin[2] · S. Autti[3] · E. Bloomfield[1] · A. Casey[2] · N. Darvishi[2] · N. Eng[2] · P. Franchini[1] · R. P. Haley[3] · P. J. Heikkinen[2] · A. Jennings[4] · A. Kemp[5] · J. March-Russell[1] · A. Mayer[3] · J. Monroe[1] · D. Muenstermann[3] · M. T. Noble[3] · J. R. Prance[3] · X. Rojas[2] · T. Salmon[3] · J. Saunders[2] · J. Smirnov[6] · R. Smith[1,2] · M. D. Thompson[3] · A. Thomson[3] · A. Ting[2] · V. Tsepelin[3] · S. M. West[2] · L. Whitehead[3] · D. E. Zmeev[3] · QUEST-DMC Collaboration

✉ E. Leason
elizabeth.leason@physics.ox.ac.uk

[1] Department of Physics, University of Oxford, Keble Road, Oxford OX1 3RH, UK

[2] Department of Physics, Royal Holloway University of London, Egham, Surrey TW20 0EX, UK

[3] Department of Physics, Lancaster University, Lancaster LA1 4YB, UK

[4] RIKEN Center for Quantum Computing, RIKEN, Wako 351-0198, Japan

[5] UKRI STFC Rutherford Appleton Laboratory, Particle Physics Department, Harwell, Didcot OX11 0QX, UK

[6] Department of Mathematical Sciences, University of Liverpool, Liverpool L69 7ZL, UK